JGR-Earth Surface

Supporting Information for

Constraining ice fabric in a fast-flowing Antarctic ice stream using icequakes

S.-K. Kufner[1*†], J. Wookey[2], A. M. Brisbourne[1], C. M. Garcia[1], T. S. Hudson[3], J. M. Kendall[3], and A. M. Smith[1]

[1]British Antarctic Survey, Natural Environment Research Council, Cambridge, UK.

[2]University of Bristol, School of Earth Sciences, Bristol, UK.

[3]University of Oxford, Department of Earth Sciences, Oxford, UK.

* Corresponding author: Sofia-Katerina Kufner (sofia-katerina.kufner@kit.edu)

† Now at the Karlsruhe Institute of Technology, Geophysical Institute, Karlsruhe, Germany

Contents of this file

Introduction

This file contains supporting information on the shear wave splitting analysis and the modeling approach introduced in the main article of this manuscript.

A detailed discussion on temporal and spatial changes in SWS parameters as well their robustness upon frequency variations is included (Text S1, Figure S1 – S2, S5 – S6). The distribution of Null measurements and the weighting function used for averaging are presented in Figures S3 and S4. Figure S7 shows the variation of inversion results dependent on the number of free parameters and Table S1 lists the model parameters for the preferred ice fabric model presented in the main text of the article.

Text S1. Temporal and spatial evolution of SWS results

We investigate the SWS results from similar azimuths and incidence angles in more detail, aiming to illuminate potential spatial or temporal variations in SWS results. Therefore, we utilize binned results, like those plotted in Figure 5. Figure S5 shows SWS measurements from four representative bins. In Figures S5 a and b, SWS parameters show some scatter (standard deviation of 0.52% and 4.3° for δV_S and Φ in a) and 0.72% and 16.5° in b)), but the variable results seem randomly distributed in map view. For instance, measurements from a similar event location, determined at the same station partly vary. Thus, the variation in SWS results likely originates from uncertainties inherited from the splitting measurement. Furthermore, some measurements (~10) in Figure S5 b are rotated by ~90°, relative to the majority of the results (~1350). This is a clear indicator that waveforms are mismatched by half a wavelength. However, this problem occurs for a few measurements only and does not severely affect the average results. On the contrary, applying a quality criterion to remove such results (e.g., based on the average value in a specific bin) might remove valid results, especially if the scatter in Φ is larger. Therefore, we decided to keep such results in the final dataset. A distribution like illustrated in Figures S5 a and b) is representative for most of the bin-wise SWS results (~95%, determined from visual inspection of all bins).

For some bins, the scatter in splitting parameters, especially of δV_S, appears distributed systematically in map view. In Figure S5 c), for instance, δV_S is smaller in the north-east of the network and larger in the south-west. The bin detailed in Figure S5 d), exhibits a spatial trend in δV_S as well. However, in this case, δV_S is larger upstream. Given these different spatial trends, it is unlikely that the spatial trend is an artefact from calculating δV_S. Notably, in both cases, the standard deviations of δV_S and Φ are in a similar range as in Figures S5 a and b (standard deviation of 0.25% and 4.4° for δV_S and Φ in c) and 0.38% and 12.5° in b)). Thus, the gentle, potentially systematic, variations of δV_S in map view are in the same range than the likely unsystematic scatter in the data and much smaller than the variations of splitting parameters with azimuth and incidence angle. Therefore, we decided to concentrate on the variation of splitting parameters with azimuth and incidence angle in this publication. The same applies for the search of potential temporal variations of splitting parameters (Subfigures ii and iii of Figure S5). The scatter of the splitting parameters at a specific time seems larger than any potential systematic temporal variations.

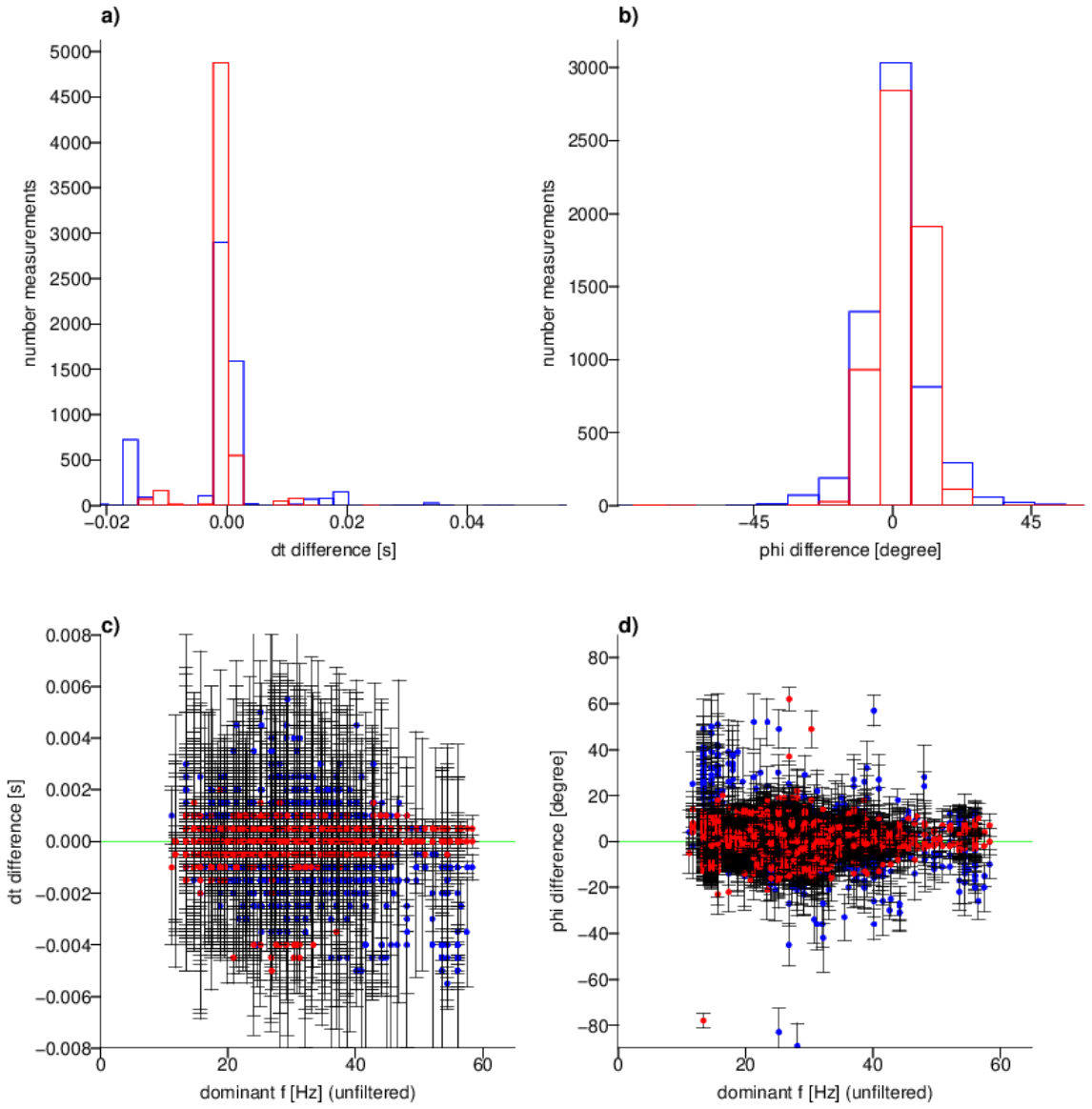

Figure S1. Comparison of SWS parameters for waveforms filtered within different frequency ranges. Red: bandpass filter between 30 and 90 Hz. Blue: bandpass filter between 20 and 40 Hz. The 'difference' refers to the results as presented in the main text of the article. a) Histogram of dt difference. Apart from a main peak around 0 (70% and 67% of all measurements for the 30-90 Hz and the 20-40 Hz band), two subpeaks around 0.015 s occur. The location of these peaks varies slightly for the two filter frequencies. Comparing waveforms from such measurements (example in Figure S2b) shows that waveforms are mismatched by roughly a cycle of the dominant frequency, which is a clear indicator for cycle skipping. b) Histogram of Φ difference. Compared to a), less spread occurs (84% and 74% of all measurements for the 30-90 Hz and the 20-40 Hz band are similar within the uncertainty range). Cycle skipping cannot be detected from the Φ difference as waveforms are mismatched by a full cycle. c) Variation of dt difference with dominant frequency of the unfiltered waveforms, excluding the events for which cycle

skipping occurs (measurements for which the dt difference is larger than 0.007 s as determined from the histogram plot in sub-figure a). Black bars indicate the uncertainty of the filtered results. Green line highlights 0 difference as reference. No clear dependence on event frequency is apparent and most (93% and 95% of all measurements for the 30-90 Hz and the 20-40 Hz band are similar within the uncertainty range) measurements are similar within their uncertainty range. d) Variation of Φ difference with dominant frequency of the unfiltered waveforms, excluding the events for which cycle skipping occurs. 96% and 75% of all measurements for the 30-90 Hz and the 20-40 Hz band are similar within the uncertainty range. As for the dt difference, no pronounced frequency dependence of the measurements is apparent.

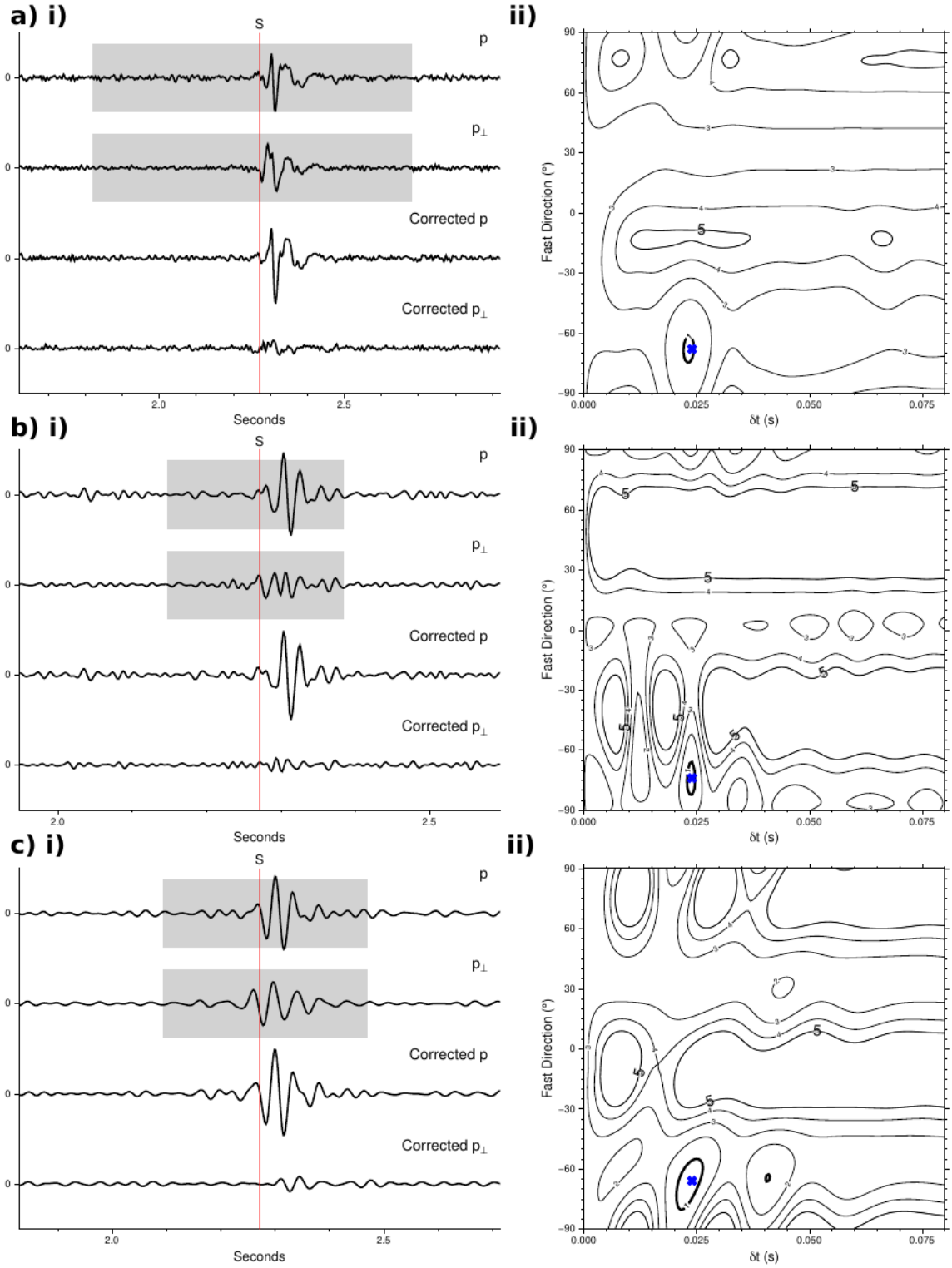

Figure S2. See caption below

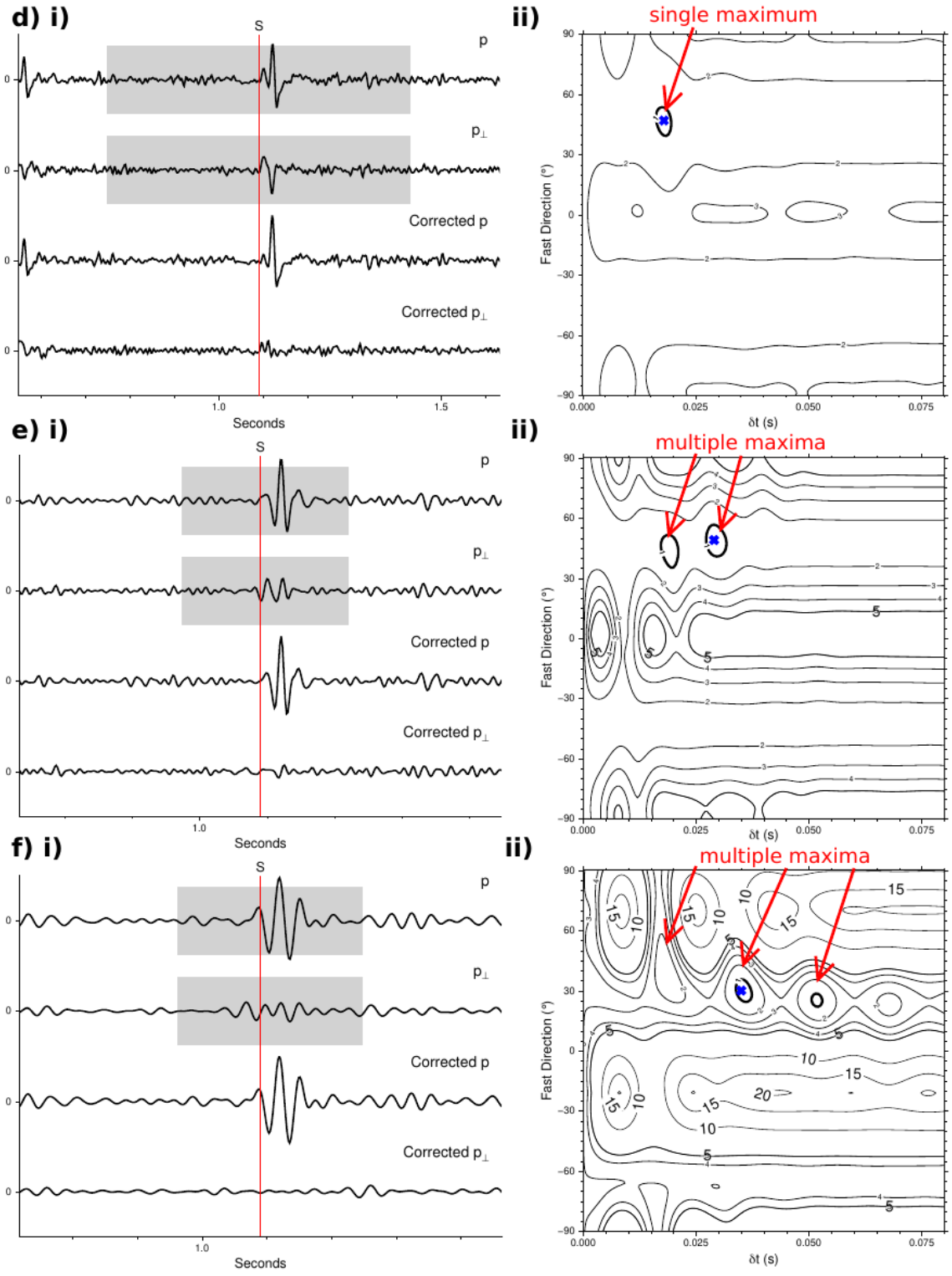

Figure S2. continued

Figure S2. SWS results at different frequencies for two example events. Subfigures i show the horizontal traces rotated into (p) and perpendicular (p⊥) to the polarization direction, which is determined in MFAST together with the splitting parameters. 'Corrected' refers to traces rotated into and perpendicular to the polarization direction after correction for the optimum anisotropy parameters. Amplitudes of the traces is normed. The splitting window is highlighted in gray, the location of the S-pick in red. Time is relative to the start of the data trace. For an optimum set of splitting parameters, the energy on 'corrected p⊥' is minimized. Subfigures ii show the misfit surface of 1/λ2'. The 95% confidence interval corresponds to the bold "1" contour. Other contours demarcate multiples of the 95% confidence interval. Contours are only shown until the tenth multiple. The optimal splitting parameters are highlighted as blue cross. a-c) Event with origin date/time 2019-01-01/05:18:06, local magnitude of –0.85, registered at a station with an epicentral distance of 2.65 km. a) shows the unfiltered waveform, b/c) show the same event filtered between 30-90 Hz and 20-40 Hz, respectively. Despite changing the frequency content, SWS results are similar within their uncertainty range. d-f) Event with origin date/time 2019-01-01/23:13:45, local magnitude of –1.37, registered at a station with an epicentral distance of 1.23 km. d) shows the unfiltered waveform, e/f) show the same event filtered between 30-90 Hz and 20-40 Hz, respectively. As highlighted by red arrows, filtering the data results in multiple maxima in the misfit surface of 1/λ2' as the fine scale structure of the waveforms is removed. Instead of the maximum with smallest dt, which would correspond to the result from d), the maxima at higher dt are more pronounced and therefore picked by the algorithm as final splitting result. Note that the maxima in f) are further apart than those in e), due to the different frequency content of the waveforms.

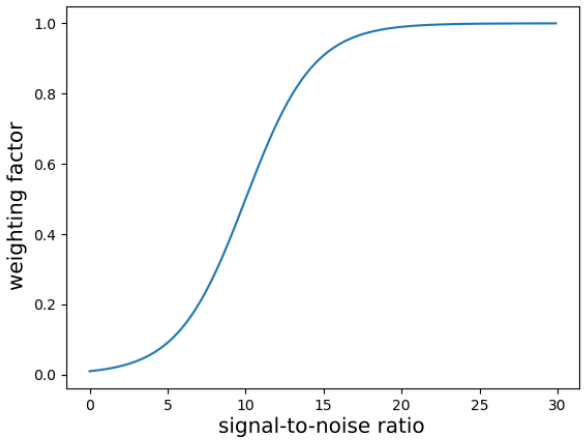

Figure S3. Weighting function for smoothed SWS results as shown in Figure 5. A weighted average of all SWS results that fall, based on similar azimuths and incidence angles, into a specific bin is calculated. Weighting is conducted based on the signal-to-noise ratio of a specific event.

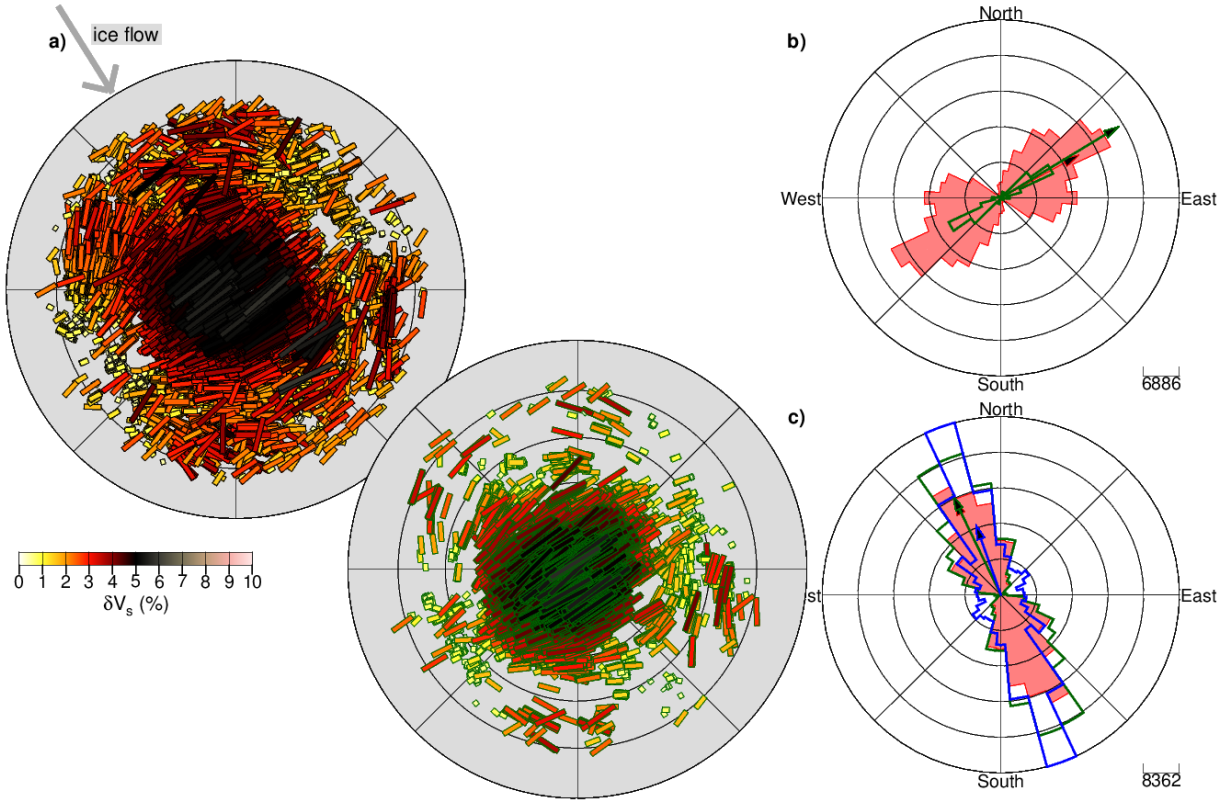

Figure S4. SWS results with Null measurements highlighted. In a) Null measurements are shown on the bottom polar plot and highlighted in dark green. All other measurements are shown in the upper polar plot. In b) and c), Φ and the initial shear wave polarization from SWS are drawn with a dark green outline. All other plotted features are as in Figure 4.

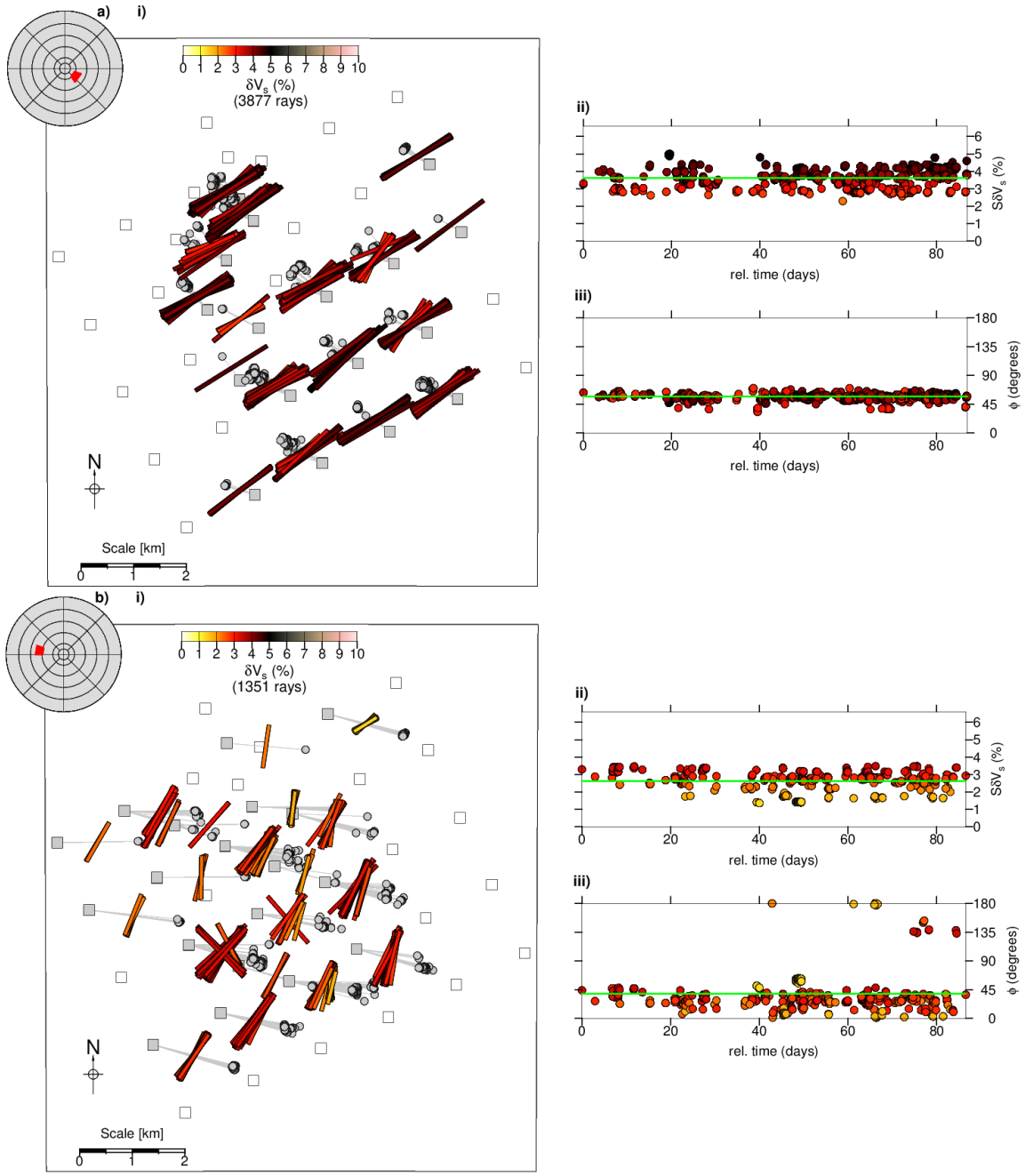

Figure S5. See caption bellow

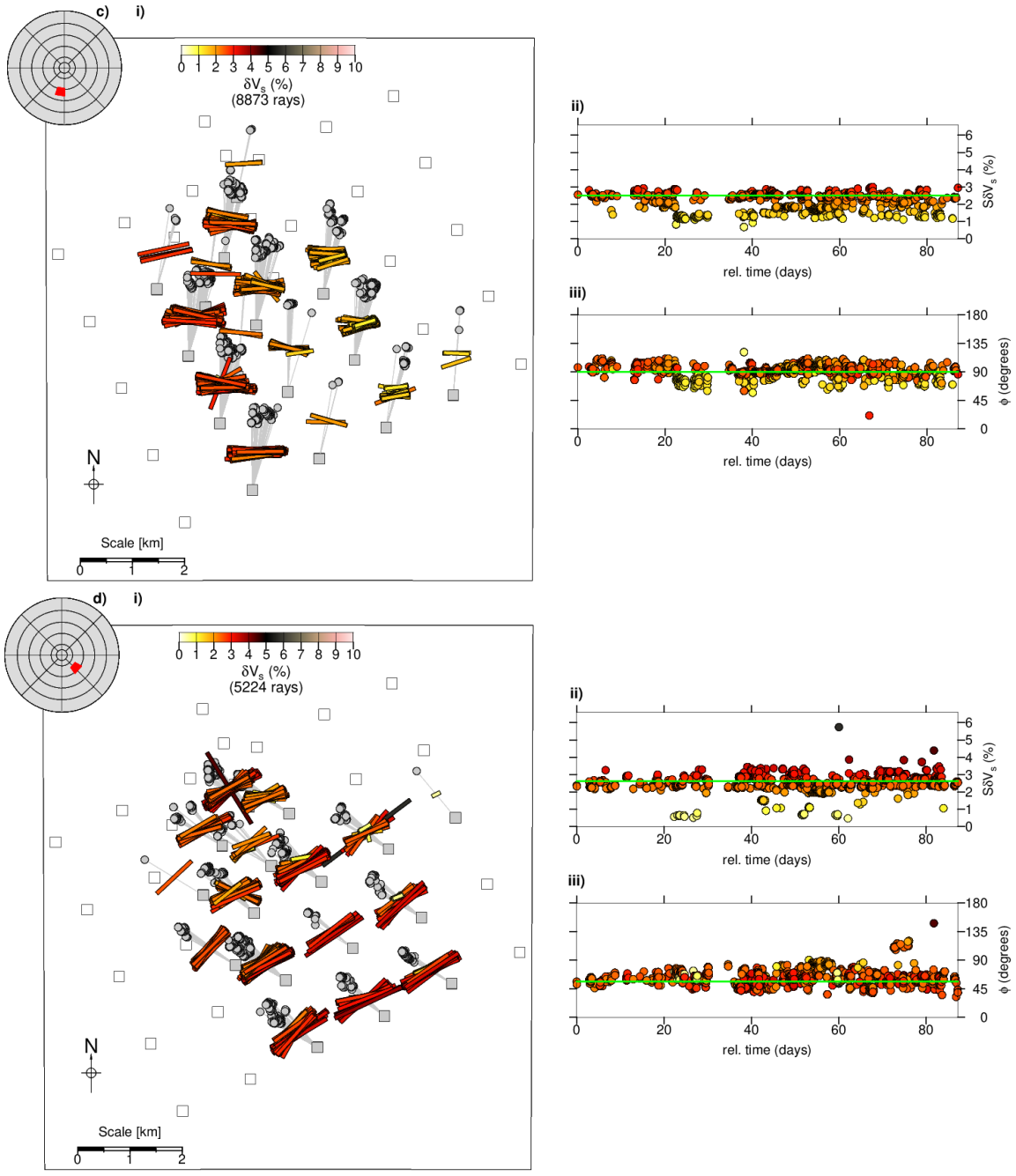

Figure S5. continued

Figure S5. Temporal and spatial variation of splitting parameters for four example bins of similar azimuths and incidence angles. In (i), the SWS parameters are plotted in map view at the mid points between event and station. Colored bars refer to percentage anisotropy, the orientation of the bars to Φ. Gray lines are ray paths, circles microseismicity and gray squares seismic stations, for which SWS measurements exist. All other stations are plotted as black squares for reference. The inset shows the location of the bin on a polar plot in the same coordinate system than plotted in Figure 5. In (ii) and (iii), the temporal evolution of δV_S and Φ is illustrated. 'rel. time' refers to the time of the first event in the specific bin. The green line highlights the average value of the specific bin. a) Bin with azimuthal range 107-145° and incidence angle range 9-16°, encompassing 3877 rays. b) Bin with azimuthal range 269-289° and incidence angle range 19-26°, encompassing 1351 rays. c) Bin with azimuthal range 179-199° and incidence angle range 19-26°, encompassing 8873 rays. d) Bin with azimuthal range 119-145° and incidence angle range 14-21°, encompassing 5224 rays.

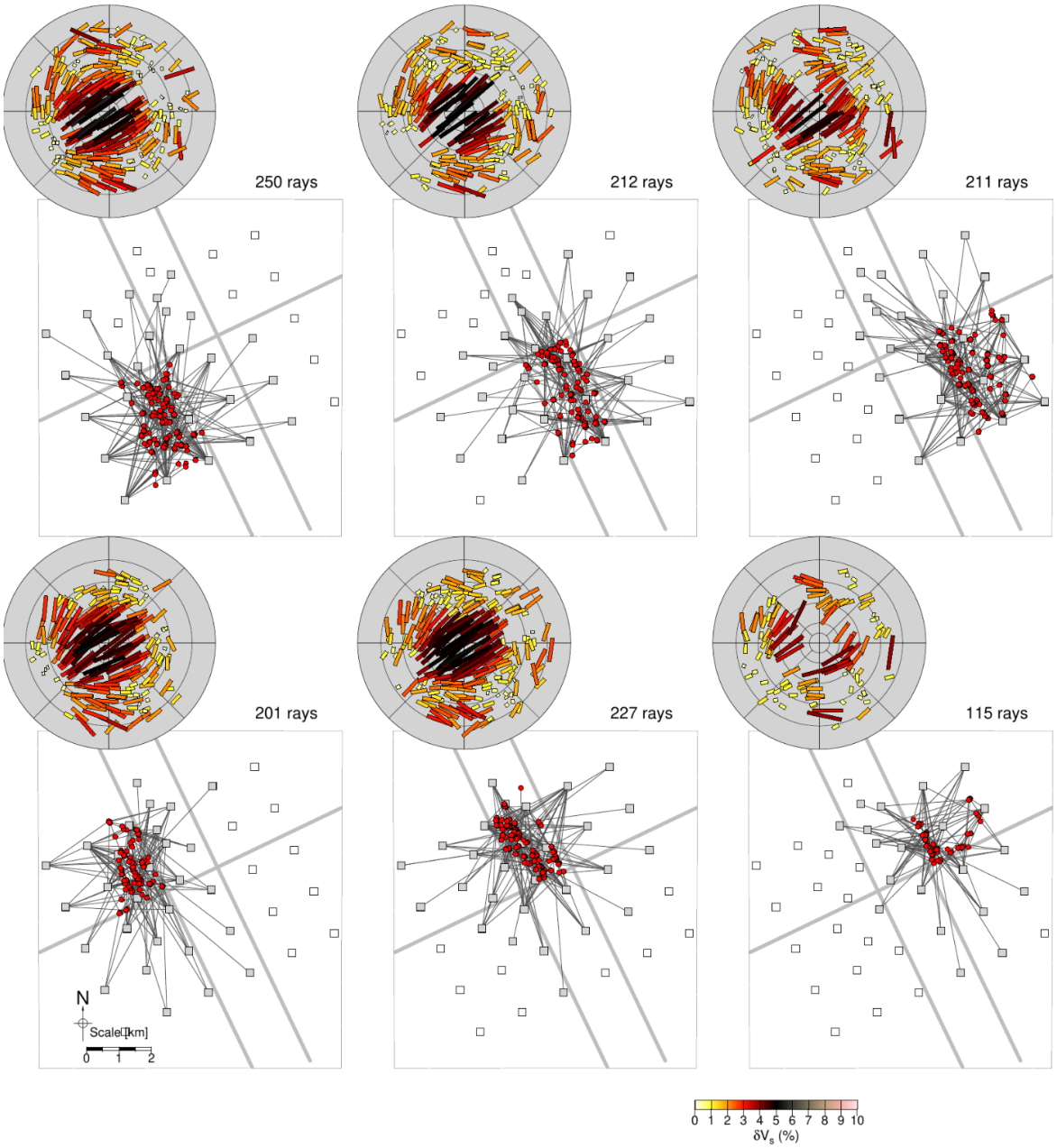

Figure S6. Input station-event pairs used for inversion on polar plots and in map view. To ensure an equal distribution of rays throughout the study region, we separate the study region into six domains. Input rays of these domains are highlighted in the six subplots. The separation between the domains is arranged parallel and perpendicular to the ice flow direction (marked by light gray lines). More details on the sampling strategy are given in the main text of the manuscript. Polar plots show splitting measurements color coded by δV_S and are in the same nomenclature and coordinate system as used in Figure 4. The maps are in the same projection as Figure 2 and highlight station (gray squares)-event (red circles) pairs used in the inversion. The total number of rays (thin gray lines) used from a specific domain is given in the top-right of each plot.

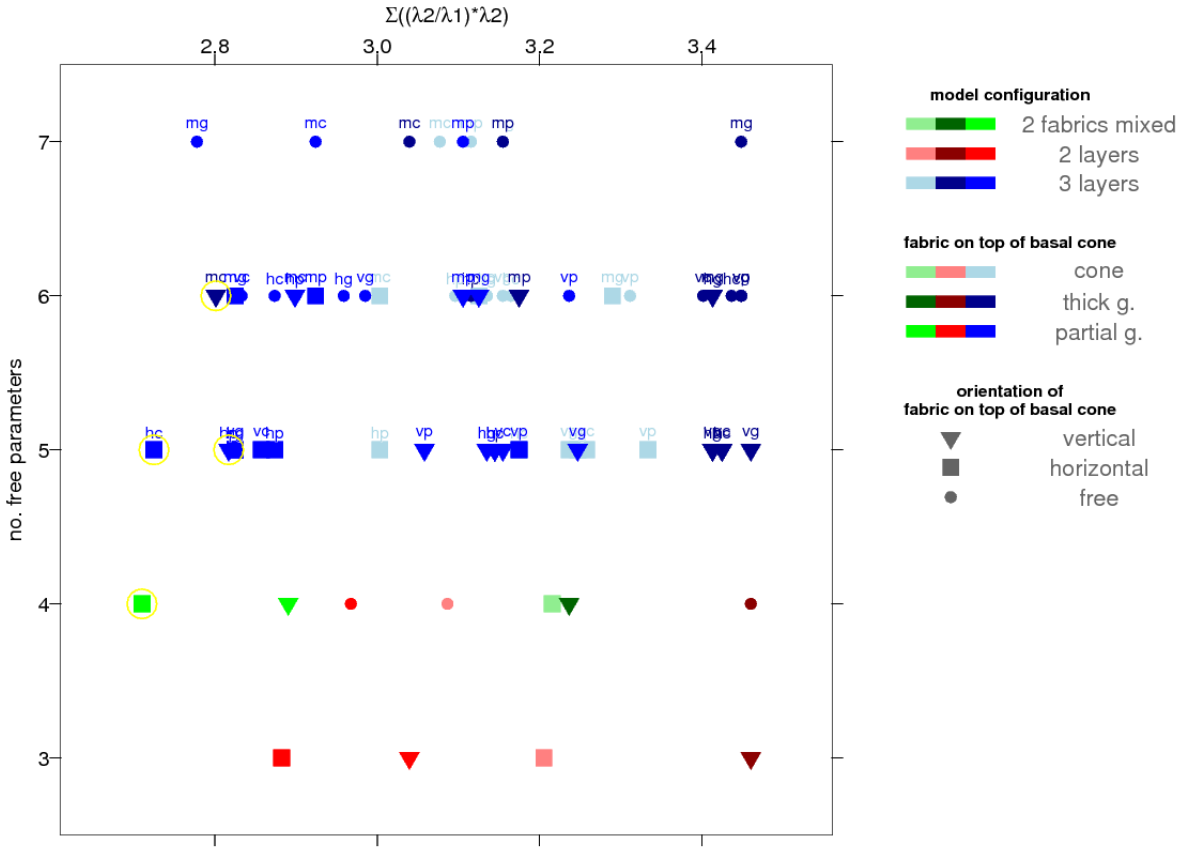

Figure S7. Comparison of inversion results relative to the number of free parameters used in the inversion. The best models described in Figures 7-9 are highlighted in yellow. See Figure 6 for an explanation of the nomenclature of the plotted symbols.

Table S1. Model parameters and uncertainty of the four models that yield the best results. See Figure 1 for a description of the angles.

a) Mixed model:
- vertical cone: opening angle of 78° (-33/+11)
- horizontal partial girdle: opening angle 23° (-6/+3) and γ 147° (-8/+7).
- mixing percentage is 52% (-32/+23) cone.

b) A three-layer model:

	Fabric	Θ (°)	α (°)	β (°)	γ (°)
Domain 1	Vertical cone	70 (-4/+14)	fixed to 0	Not used	fixed to 0
Domain 2	Vertical partial girdle	49 (-3/+4)	fixed to 0	Not used	148 (-6/+5)
Domain 3	Horizontal partial girdle	21 (-4/+2)	fixed to 90	Not used	150 (-10/+5)

c) A three-layer model:

	Fabric	Θ (°)	α (°)	β (°)	γ (°)
Domain 1	Vertical cone	82 (-41/+7)	fixed to 0	Not used	fixed to 0
Domain 2	Horizontal partial girdle	22 (-2/+3)	fixed to 90	Not used	144 (-5/+11)
Domain 3	Horizontal cone	80 (-20/+9)	fixed to 90	Not used	137 (-24/+115)

d) A three-layer model:

	Fabric	Θ (°)	α (°)	β (°)	γ (°)
Domain 1	Vertical cone	87 (-36/+1)	fixed to 0	Not used	fixed to 0
Domain 2	Vertical thick girdle	16 (-14/+21)	Not used	fixed to 0	143 (-19/+18)
Domain 3	Tilted cone	9 (-9/+15)	51 (+6/-7)	Not used	143 (-6/+18)